Barotropic and Moisture–Vortex Growth of Monsoon Low Pressure Systems

HAOCHANG LUO,[a] ÁNGEL F. ADAMES CORRALIZA,[a,b] AND RICHARD B. ROOD[a]

[a] Department of Climate and Space Sciences and Engineering, University of Michigan, Ann Arbor, Michigan
[b] Department of Atmospheric and Oceanic Sciences, University of Wisconsin–Madison, Madison, Wisconsin

(Manuscript received 1 December 2022, in final form 28 September 2023, accepted 6 October 2023)

ABSTRACT: As one of the most prominent weather systems over the Indian subcontinent, the Indian summer monsoon low pressure systems (MLPSs) have been studied extensively over the past decades. However, the processes that govern the growth of the MLPSs are not well understood. To better understand these processes, we created an MLPS index using band-pass-filtered precipitation data. Lag regression maps and vertical cross sections are used to document the distribution of moisture, moist static energy (MSE), geopotential, and horizontal and vertical motions in these systems. It is shown that moisture governs the distribution of MSE and is in phase with precipitation, vertical motion, and geopotential during the MLPS cycle. Examination of the MSE budget reveals that longwave radiative heating maintains the MSE anomalies against dissipation from vertical MSE advection. These processes nearly cancel one another, and it is variations in horizontal MSE advection that are found to explain the growth and decay of the MSE anomalies. Horizontal MSE advection contributes to the growth of the MSE anomalies in MLPSs prior to the system attaining a maximum amplitude and contributes to decay thereafter. The horizontal MSE advection is largely due to meridional advection of mean state MSE by the anomalous winds, suggesting that the MSE anomalies undergo a moisture–vortex instability (MVI)-like growth. In contrast, perturbation kinetic energy (PKE) is generated through barotropic conversion. The structure, propagation, and energetics of the regressed MLPSs are consistent with both barotropic and moisture–vortex growth.

KEYWORDS: Indian Ocean; Convection; Monsoons; Kinetic energy; Moisture/moisture budget

1. Introduction

Westward- or northwestward-propagating synoptic-scale disturbances are frequently observed over the Bay of Bengal during the summer monsoon season. Often referred to as monsoon low pressure systems (MLPSs), these systems exhibit a horizontal structure of roughly 2000 km across and extend vertically from the surface to 100 hPa (Godbole 1977; Sikka 1977; Krishnamurti et al. 1975; Adames and Ming 2018a). From June to September, around 2–4 MLPSs form per month on average (Krishnamurti et al. 2013; Thomas et al. 2021, 2022). In spite of their short 3–5-day life cycle, they play an important role in the hydrologic cycle of South Asia, accounting for up to 50% of the summer monsoon rainfall (Krishnamurti 1979; Saha et al. 1981; Yoon and Chen 2005; Yoon and Huang 2012; Thomas et al. 2021). The variation of precipitation brought about by MLPSs significantly impacts agriculture and fishery (Dong et al. 2017; Thomas et al. 2021). It is not only a major source of freshwater to one of the most densely populated areas of the world, but it is also a major cause of life-threatening floods, as previous studies have documented (Ajayamohan et al. 2010; Hunt et al. 2018; Hunt and Fletcher 2019).

Although MLPSs have been extensively documented, the mechanisms responsible for their growth and propagation have remained elusive. MLPSs are situated in a vertically sheared environment that is conventionally thought to favor baroclinic instability (Charney and Stern 1962; Krishnamurti et al. 1976, 2013). As a result, previous studies hypothesized that baroclinic instability (Rao and Rajamani 1970; Saha and Chang 1983), often enhanced by cumulus heating (Moorthi and Arakawa 1985; Krishnakumar et al. 1992; Kasture et al. 1993), or baroclinic–barotropic instability can excite and amplify these systems (Aravéquia et al. 1995). However, major disagreements between observations and theory have made the idea of baroclinic growth in MLPSs questionable (Cohen and Boos 2016). Vertical cross sections of potential vorticity documented in previous studies show upright or slightly westward tilted structures and neither of the two is characteristic of baroclinic instability under easterly shear. Results from idealized simulations of MLPSs also agree that baroclinic instability does not explain MLPS growth (Diaz and Boos 2019a; Clark et al. 2020). Also, Moorthi and Arakawa (1985) showed that a weak vertical shear, along with a weak meridional temperature gradient at lower levels, does not favor baroclinic instability when cumulus heating is absent.

With baroclinic instability unlikely to be the source of growth of MLPSs, alternative hypotheses have been proposed. One potential theory, namely, is the moisture–vortex instability (MVI) (Adames and Ming 2018a). As a generalization of the balanced moisture waves described by Sobel et al. (2001), MVI emphasizes the role of prognostic moisture in MLPS-related rainfall and horizontal gradients of moisture and temperature in MLPS growth (Fig. 1; Adames 2021). As one of the emblematic features, the meridional advection of moist static energy (MSE) induces a moisture tendency to the west of the MLPSs. The convection is then enhanced by the anomalously high moisture, which peaks near or slightly to the west of the center of the

---

Corresponding author: Haochang Luo, hcluo@umich.edu

DOI: 10.1175/JAS-D-22-0252.1

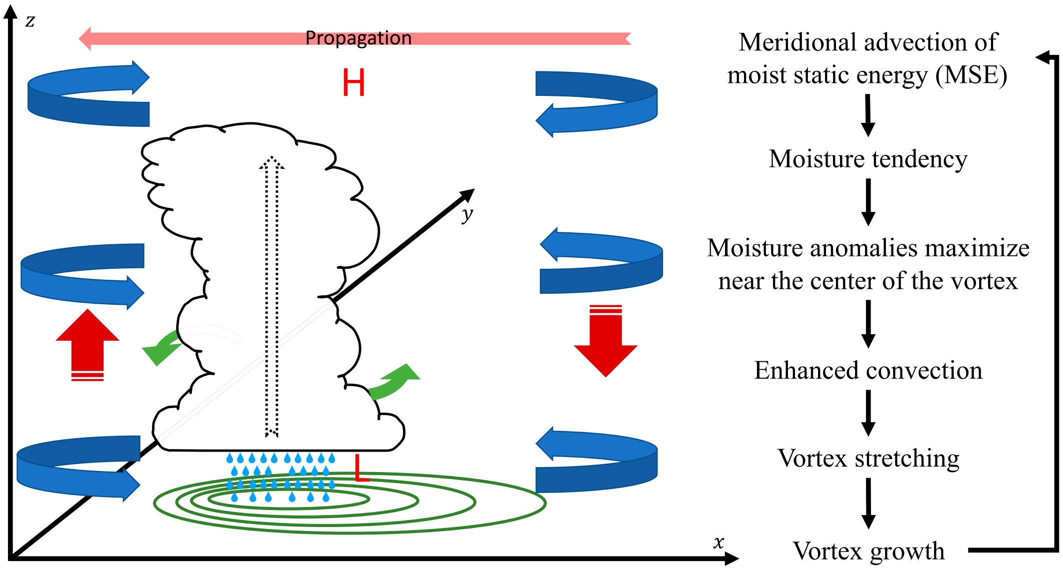

FIG. 1. (left) Schematic of moisture–vortex instability. The light red arrow on the top refers to the westward propagation. The blue curved arrows represent the circulations at low, mid-, and high levels, with a high pressure on the top and a low pressure on the bottom. The meridional MSE advection is shown as the green arrows. The dark red upward (downward)-pointing arrow refers to the adiabatic lifting (subsidence). The contours near the surface represent a high column moisture center, which is partly collocated with the precipitation. The dashed arrow is enhanced convection. (right) A flowchart showing this mechanism.

vortex. Last, the vortex strengthens due to vortex stretching. Adames (2021) recently posited that MVI is amplified over South Asia at the expense of baroclinic instability, potentially explaining why baroclinic instability is not observed in this region.

The South Asian monsoon is also characterized by strong meridional shears in the zonal wind that allow it to be barotropically unstable (e.g., Lindzen et al. 1983; Nitta and Masuda 1981). However, dry barotropic instability alone does not provide adequate energy to allow MLPSs to grow against dissipation (Diaz and Boos 2019a). As a result, it has been hypothesized that a variant of barotropic instability that includes moist processes, termed moist barotropic instability, can explain MLPS growth (Diaz and Boos 2019a,b). Although the explanations for how diabatic heating enhances the vortex are different, the theory still shares some similarities with MVI. For example, the low-level meridional MSE gradient is still a primary energy source and the moisture advected by the winds toward the vortex enhances the convection (Diaz and Boos 2021a).

In this paper, we will examine the energetics of MLPSs in order to elucidate the processes that may be able to explain their growth. Because we are investigating barotropic and moisture–vortex instabilities, we will emphasize the moist static and perturbation kinetic energy budgets. The contents are structured as follows: the data and methods used in this study are shown in section 2. The climatological features of monsoons and disturbances are depicted in section 3. Section 4 is the analysis on MVI and barotropic instability energetics. Concluding remarks are shown in section 5.

2. Data and methods

The data used in this study are the fifth reanalysis product from the European Centre for Medium-Range Weather Forecasts (ERA5; Hersbach et al. 2019). We examined the MLPSs from 1980 to 2019 for the extended boreal summer, June to September (JJAS), when MLPSs are the most active. The temporal resolution is 6 h, the spatial resolution is 0.5° × 0.5° in longitude and latitude, and there are 27 layers ranging from 1000 to 100 hPa in the vertical direction.

Our analysis is based on linear regressions onto an MLPS index. Different indices were used to represent MLPS activity in previous studies for different purposes (Boos et al. 2015; Ditchek et al. 2016). In this study, we put emphasis on rainfall-related features, so our index is based on precipitation anomalies that are filtered in space and time and regionally averaged over a spot with strong rainfall variabilities (Hayashi 1971, 1979; Wheeler and Kiladis 1999; Wheeler et al. 2000). The applied filter retains data between westward zonal wavenumbers 3 and 25, and frequencies between 1/15 and 1/2 day^{-1}, where the strongest signal shows up on the wavenumber–frequency diagrams (Adames and Ming 2018b). The outputs were then averaged over a box area, 85°–90°E, 15°–20°N (red box in Figs. 2a,b) (Sikka 1977; Godbole 1977; Boos et al. 2015; Adames and Ming 2018b). This location has a high precipitation rate and variance. It is also the place for maximum MLPS genesis (Krishnamurthy and Ajayamohan 2010; Boos et al. 2016). The index was then standardized by subtracting its temporal average and dividing by the temporal standard deviation. We have verified that similar results are obtained if an alternative index based on the sea level pressure is used as a time series or

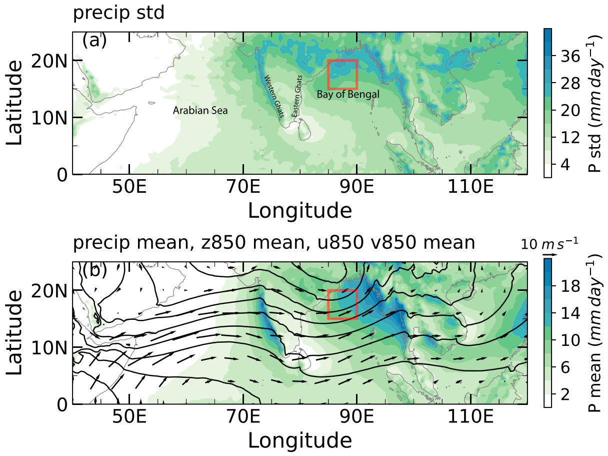

FIG. 2. (a) Standard deviation of JJAS mean total precipitation rate. The MLPS index was calculated by averaging the precipitation anomalies over the area within the red box. (b) JJAS mean precipitation (shadings), geopotential height (contours, starting from 1440 to 1540 gpm, at an interval of 10 gpm), and winds at 850 hPa (vectors).

if EOF analysis is used instead in the appendix. Statistical significance of the regression fields is determined by a two-tailed t test (Davis 1978; Chen 1982; Adames and Wallace 2014) at a level of 95%. Only anomaly fields that are found to be statistically significant according to this test are shown.

Most of the fields were integrated through the atmospheric column. The mass-weighted vertical integrals were calculated using the following equation (Adames and Ming 2018b):

$$\langle \square \rangle = -\frac{1}{g}\int_{p_s}^{p_t} \square \, dp, \qquad (1)$$

where $g = 9.8$ m s^{-2} is the gravitational acceleration, $p_t = 100$ hPa and $p_s = 1000$ hPa are seen as the tropopause and surface pressures, respectively, and the open square "□" represents an arbitrary quantity.

Our study focuses on the MSE and perturbation kinetic energy (PKE) of MLPSs. The MSE is defined as

$$m = C_p T + \Phi + L_v q, \qquad (2)$$

where m is the MSE, $C_p = 1004$ J (K kg)$^{-1}$ is the heat capacity at constant pressure, T is the temperature, Φ is the geopotential, $L_v = 2.5 \times 10^6$ J kg^{-1} is the specific latent heat, and q is the specific humidity. The sum of the first two terms is the dry static energy (DSE).

The PKE is defined as

$$K' = \frac{1}{2}(u'^2 + v'^2), \qquad (3)$$

where K' is the PKE and u' and v' are the zonal and horizontal wind temporal anomalies obtained through the filtering process. In this paper, we use the prime symbol to represent the anomalies in time and the overbar symbol to represent the background state in which the anomalies propagate.

3. Characteristics of monsoon low pressure systems

To better understand the processes that govern the evolution of MLPSs, it is instructive to first consider the climatology of the South Asian monsoon, shown in Fig. 2. The Bay of Bengal, where MLPS activity is the strongest, is characterized by average precipitation rates that exceed 4 mm day^{-1} (Fig. 2b). The rainfall maxima are on the west coast of India and central India as well as on the eastern and northern Bay of Bengal. Our indexing area is to the east of the monsoon trough, with a precipitation rate standard deviation higher than 20 mm day^{-1} (Fig. 2a). In Fig. 2b, a low-level westerly jet shows up at around 10°–20°N at 850 hPa. The westerlies peak near 60°E and slow down when encountering the Western Ghats at 75°E and the Eastern Ghats at 80°E. Then, they speed up when entering the Bay of Bengal.

The disturbances and related precipitation (P') that grow in this background state are shown in Fig. 3. The lag regressions were calculated from 2 days before (day −2) the maximum signal to 2 days after (day 2). At 850 hPa, anomalous anticyclones are collocated with suppressed precipitation and enhanced precipitation is in phase with the anomalous cyclones. Although the circulation and the precipitation anomalies are generally collocated with each other, there is a small displacement between the two fields with rainfall centers shifted toward the southwest of the troughs and ridges. Individual highs and lows move across 15° westward while only 5° northward.

On day −2, the centers of the negative precipitation anomalies are located near the eastern coast of India and the positive anomalies are centered over the eastern Bay of Bengal. From day −2 to day 0, the positive precipitation anomalies amplify. On day 0, the negative precipitation anomalies are located in northwestern India and the positive anomalies are centered over the northwestern Bay of Bengal. From day 1 to day 2, the positive center and the negative center to the west weakened, while the newly developing negative center on the east intensified along with the anticyclonic flow. On day 2, the locations of the centers are the same as on day −2 but with a reversed pattern.

The lag regressions of anomalous column-integrated MSE exhibit a similar pattern as the rainfall anomalies (not shown). Their root-mean-square amplitude is shown as the contours in Fig. 4. The shading shows the climatological mean column-integrated MSE. Mean MSE increases from southwest to northeast and peaks near 25°N, 90°E. The contours show the west-northwestward propagation of the MLPSs, which approximately follows the contours of mean MSE from ~70° to 105°E.

The longitude–height cross sections of meridionally averaged (5°–20°N) geopotential height, winds, moisture, and MSE are shown in Fig. 5. The vertical distribution of geopotential height (contours) is upright during growth and tilts westward with height when it decays, consistent with previous findings (Godbole 1977; Hunt et al. 2016; Cohen and Boos 2016). The negative anomalous latent energy (left shadings) had a maximum near 500 hPa in the growing stage, while it is

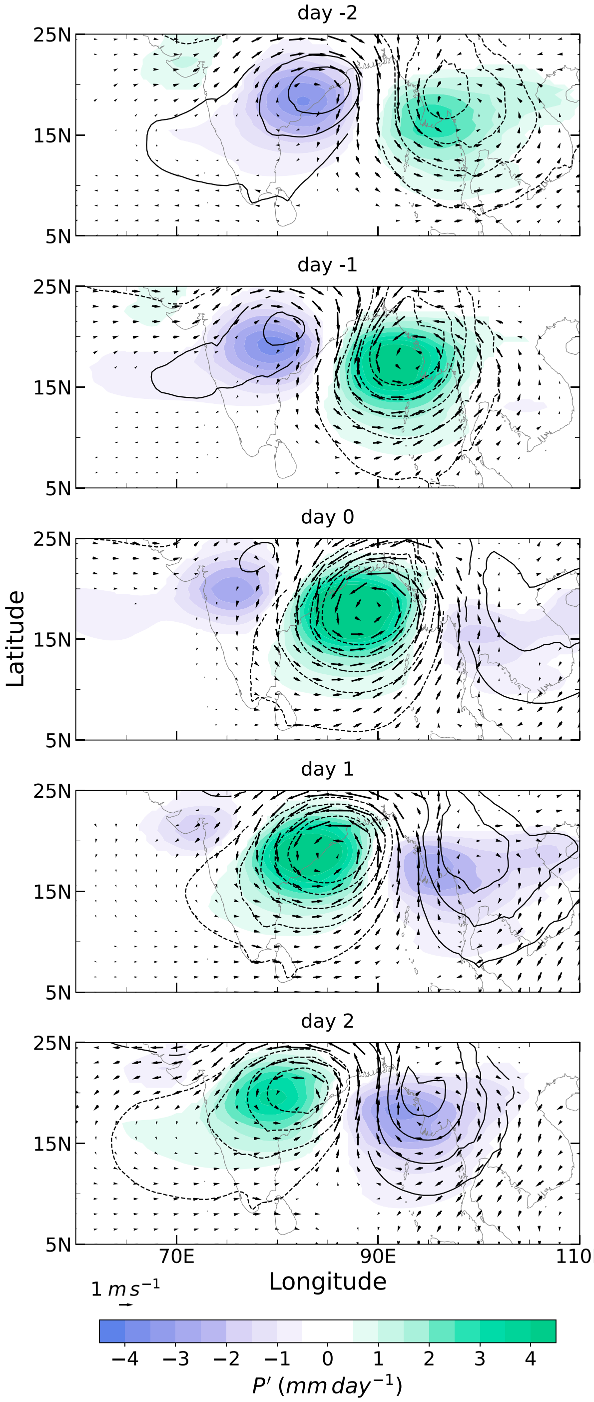

FIG. 3. Lag regressions from (top) day −2 to (bottom) day 2 of anomalous precipitation rate (shadings), geopotential height (contours, starting from −4 to 4 gpm at an interval of 1 gpm), and winds (vectors) at 850 hPa onto the MLPS index during JJAS. Only statistically significant anomalies are shown.

around 800 hPa during its decay. The negative anomalous MSE (right shading), however, persisted at 500 hPa. The structure of enhanced latent energy and MSE is similar. The vertical wind anomalies (u, ω, shown as vectors in Fig. 5, with ω scaled for better display) exhibit an upward motion within the positive moisture and MSE anomalies while downward motion in the negative MSE anomalies.

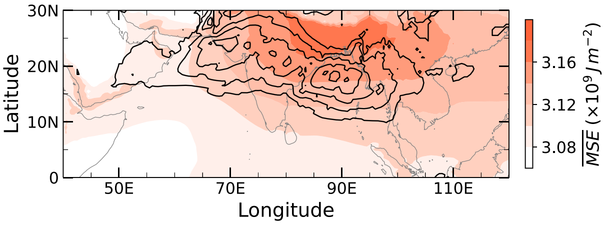

FIG. 4. Column-integrated mean MSE is shown as shading. The contours are the root-mean-square of anomalous MSE regressed onto the MLPS index from day −2 to day 2 (from 0 to 30 × 10^9 J m^{-2} at an interval of 5 × 10^9 J m^{-2}).

As discussed in the previous sections, the upright structure shown in the vertical cross sections is inconsistent with baroclinic instability, which requires an eastward tilt with height. The peaks of column moisture and the precipitation anomalies, shown in Fig. 6, are collocated with each other near 88°E. To better present, the values are standardized by subtracting their temporal averages and then dividing by standard deviations. The anomalous ascent is shifted about 3° westward with respect to the other two fields. The vertical structure and shift shown in Fig. 6 are consistent with MVI as shown in Fig. 14 of Adames (2021). The upright structure in geopotential and horizontal winds is also consistent with barotropic growth.

4. Energetics

a. *Moist static energy budget*

In this section, we will investigate MSE and PKE budgets and show the major possible contributors to the growth and propagation of MLPSs. Following Adames and Ming (2018b), the tendency of MSE can be broken down into the following terms:

$$\frac{\partial \langle m' \rangle}{\partial t} = -\left\langle u\frac{\partial m}{\partial x}\right\rangle' - \left\langle v\frac{\partial m}{\partial y}\right\rangle' - \left\langle \omega\frac{\partial m}{\partial p}\right\rangle' + \mathrm{LW}' + \mathrm{SW}' + \mathrm{SH}' + L_v E', \qquad (4)$$

where the prime refers to the anomalies obtained with a 1/2 to 1/15 day^{-1} bandpass filter (see section 2). Angle brackets represent mass-weighted column integration [Eq. (1)]. The term on the left-hand side is the anomalous MSE tendency. On the right, $u(\partial m/\partial x)$ is the zonal advection of anomalous MSE, $v(\partial m/\partial y)$ is the meridional advection, $\omega(\partial m/\partial p)$ is the vertical advection, LW is the net longwave radiation flux, SW is the net shortwave radiation flux, SH is the surface sensible heat flux, and $L_v E$ is the surface latent heat flux. All the flux terms are positive upward.

To elucidate the processes that lead to the propagation and growth of MSE anomalies in MLPSs, the fractional contributions to the tendency and maintenance ($\langle m' \rangle$) of anomalous MSE from each term in Eq. (4) are shown in Fig. 7. The variance contributions were defined using the following equation (Andersen and Kuang 2012):

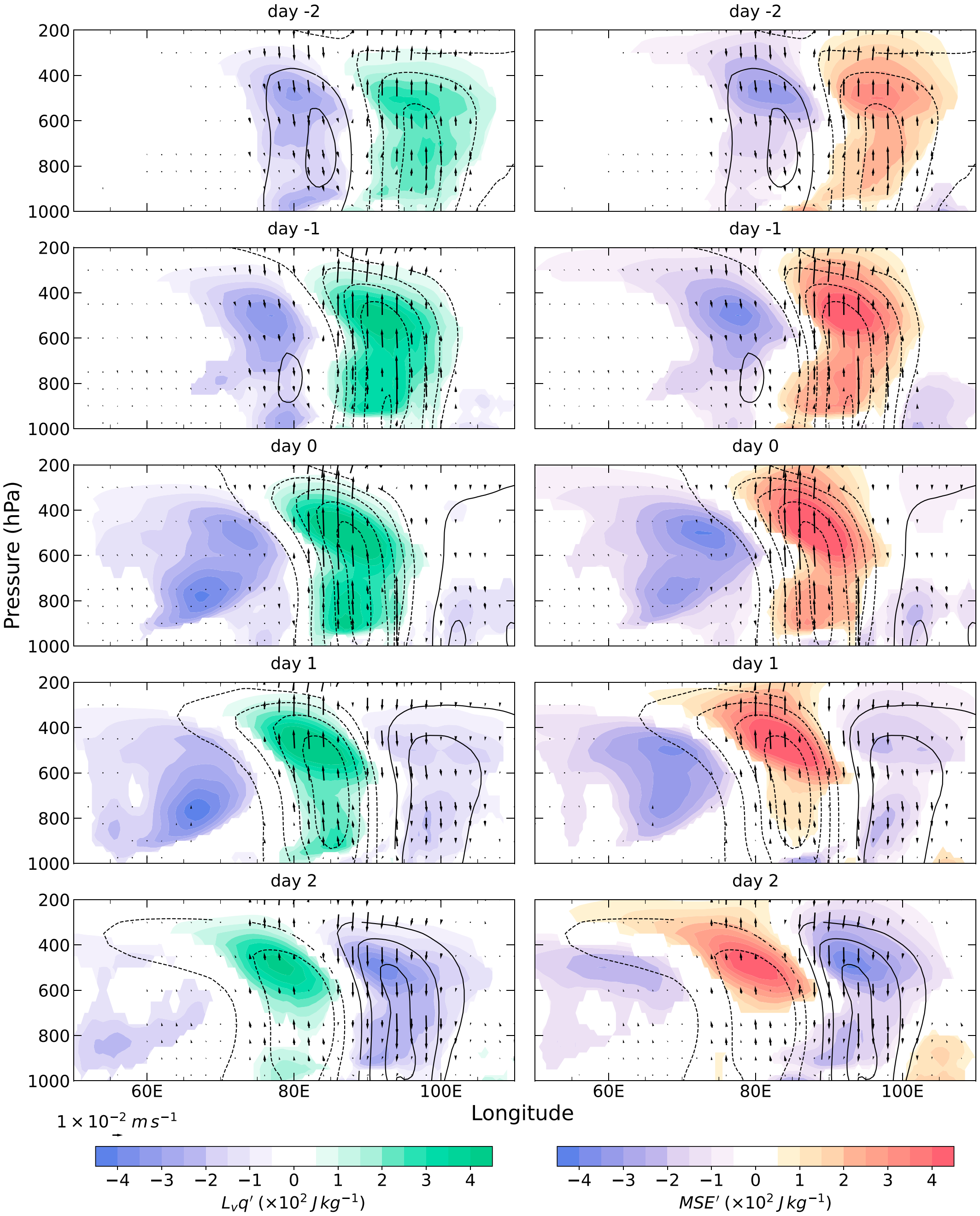

FIG. 5. Longitude–height cross sections of (left) anomalous latent energy (L_vq'; shading) and (right) MSE (shading) along with geopotential height (contours, from −5 to 5 gpm at an interval of 1 gpm) and zonal and vertical wind (vectors; vertical winds are scaled to a larger magnitude) anomalies regressed onto the MLPS index from (top) day −2 to (bottom) 2 during JJAS. Averaged over 10°–25°N. Only statistically significant anomalies are shown.

$$C = \frac{\sum_{i=1}^{n} X_i Y_i}{\sum_{i=1}^{n} Y_i^2}, \tag{5}$$

where C refers to the percentage of variance explained by X with respect to Y, n is the total number of the grid points in the domain, X is the right-hand side terms in the budget equations, Y can be either $\partial\langle\square\rangle/\partial t$ (tendency) or $\langle\square\rangle$ (maintenance), and the open square ($\square$) is either anomalous MSE or PKE. The contributors to tendency can be interpreted as the mechanism responsible for propagation, and the contributors to maintenance correspond to intensity variations.

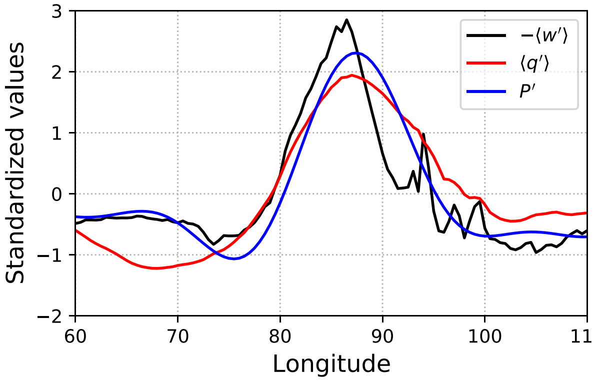

FIG. 6. Column-integrated anomalous vertical velocity (black), moisture (red), and precipitation (blue), zonally averaged across 10°–25°N on day 0. The values are standardized as discussed in section 3.

As is shown in Fig. 7, the overwhelming contribution to the MSE tendency comes from the meridional MSE advection. It peaks at day 0, and the lead and lag regressions are nearly symmetric with respect to day 0. Other terms contribute little. The relative contribution of each term to the MSE tendency changes little from day −2 to day 2.

Unlike the contributions to the MSE tendency, the contributors to MSE maintenance exhibit pronounced changes from day −2 to day 2. The positive projection of MSE time tendency to the maintenance illustrates the growth and the negative represents the decay of the depressions. The system grows on day −2 and day −1. It starts weakening on day 0. The decaying process accelerates on day 1, with dissipation occurring on day 2, the same day that a new vortex forms to the east (Fig. 5).

The leading contributors to MSE maintenance are horizontal MSE advection, vertical MSE advection, and longwave radiative heating (bottom panel of Fig. 7). The longwave radiative heating contribution is due to an anomalous greenhouse effect that arises from the presence of anomalous high clouds in the MLPS, acting as an MSE source (Andersen and Kuang 2012; Wolding et al. 2016; Adames and Ming 2018b). The vertical MSE advection is an MSE sink in MLPSs because the rate of large-scale condensation exceeds the moistening by vertical moisture advection. When examined together, we see that longwave radiative heating and vertical MSE advection change little from day −2 to day 2 and approximately cancel each other out. In contrast, the horizontal MSE advection terms vary in time with the MSE tendency. During days −2, −1, and 2, the growth is predominantly determined by the meridional MSE advection, while the decay during day 0 is related to zonal MSE advection and the decay on day 1 is due to both zonal and meridional advection. Although small, surface latent heat fluxes do still contribute to MSE maintenance.

Horizontal maps of the largest contributors to the MSE propagation and maintenance are shown in Fig. 8. As in Fig. 7, we see that the positive meridional advection of MSE shows up to the west of the enhanced MSE anomalies. The pattern is collocated with the MSE tendency anomalies, corroborating that the propagation of MLPSs is largely determined by the anomalous meridional advection of MSE. Additionally, on days −2 and −1, the center of enhanced MSE anomalies has a larger overlap with the positive meridional MSE advection than with the negative advection, indicating the growth of the system. The meridional MSE advection becomes negative on day 1 contributing to the decay of MLPS. We also see more clearly that the vertical MSE advection and LW′ are in phase with the MSE anomalies and tend to cancel one another.

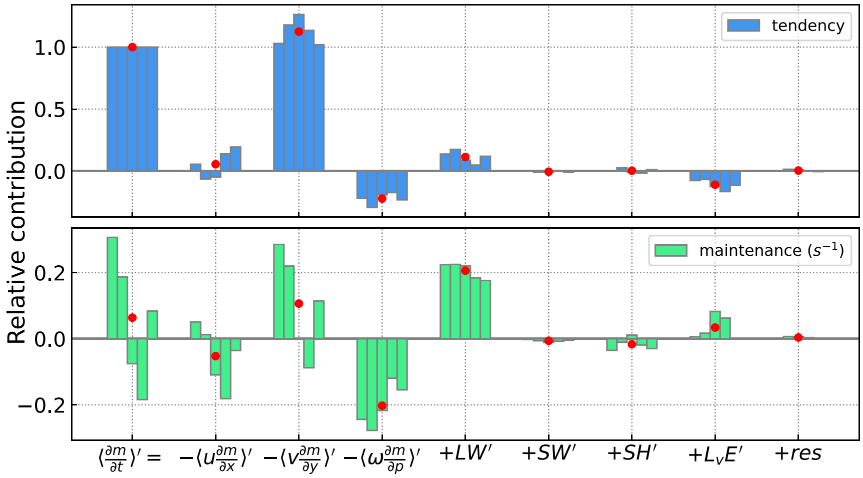

FIG. 7. Normalized contributions to (top) MSE tendency ($\partial \langle m' \rangle / \partial t$) and (bottom) maintenance ($\langle m' \rangle$) from the terms in Eq. (4). "Res" is the residual between the left-hand side and the right-hand side. The five bins within each group represent the lag regressions at days −2, −1, 0, 1, and 2 during JJAS. The red dots are the averages of the 5 days. The contributions are calculated within 60°–110°E, 10°–25°N.

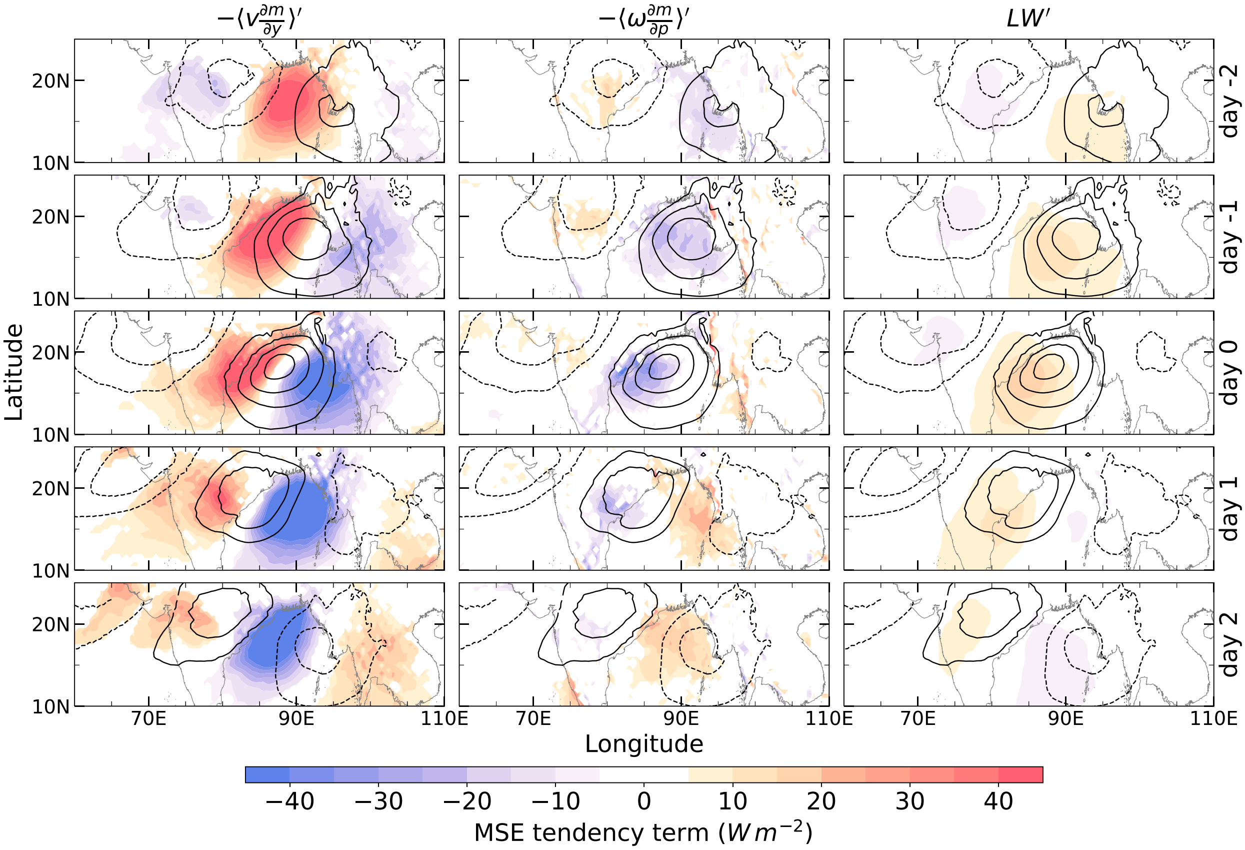

FIG. 8. From top to bottom, the maps are lag regressions from day −2 to day 2. From left to right, the shadings are column-integrated meridional MSE advection [$-\langle v(\partial m/\partial y)\rangle'$], vertical MSE advection [$-\langle \omega(\partial m/\partial p)\rangle'$], and longwave radiation flux anomalies (LW′). The contours are column-integrated anomalous MSE ($\langle m'\rangle$, from -2×10^6 to 4×10^6 J m^{-2} at an interval of 1×10^6 J m^{-2}). Only statistically significant anomalies are shown.

To better understand how the MSE is advected horizontally, we decompose the advection into contributions from the anomalies and from the background state, i.e., $\langle(\overline{v} + v')\partial_y(\overline{m} + m')\rangle$. Through this decomposition, we find that the meridional advection of background MSE by the anomalous winds governs the meridional MSE advection, making up over 90% of it:

$$\left\langle v\frac{\partial m}{\partial y}\right\rangle' \simeq \left\langle v'\frac{\partial \overline{m}}{\partial y}\right\rangle. \qquad (6)$$

In Fig. 9a, we see that $v(\partial m/\partial y)$ and $v'(\partial \overline{m}/\partial y)$ are in phase with each other. Thus, the propagation and growth of the MSE in the MLPS can be qualitatively understood by how its anomalous winds advect the monsoonal distribution of MSE. The background MSE ($\overline{m}$) is further decomposed into latent energy ($L_v q$) and DSE contributions (Fig. 9b). In contrast to the general circulation model results in Adames and Ming (2018b), the anomalous moisture advection is the major contributor to the anomalous MSE advection in ERA5. The meridional latent energy advection makes up over 75% of the meridional MSE advection. The zonal latent energy advection makes up an even larger fraction of the zonal MSE advection. Thus, the horizontal MSE advection in MLPSs is largely due to horizontal moisture displacements.

b. *Perturbation kinetic energy budget*

Linear regressions of column-integrated perturbation kinetic energy K' are shown in Fig. 10. Positive PKE is observed in association with the anomalous cyclone, implying that PKE increases with the passage of these systems. On the other hand, negative PKE is seen with the anomalous anticyclones, implying that PKE is reduced during the passage of these systems. A west-northwest propagation of the PKE anomalies is seen, consistent with the propagation of the MSE anomalies discussed previously. On day −2, the negative PKE center is seen to the northeast of the anticyclonic flow. The positive PKE is centered substantially farther east of the cyclonic flow, near the South China Sea. On day −1, this center weakens and positive PKE develops to the east of the center of the anomalous cyclone. During the following days, the anomalous centers are on the northeast of the geopotential height centers. Contrary to the precipitation and MSE anomalies, the centers of PKE shift slightly northeastward of the geopotential centers, collocating within the strongest horizontal wind anomalies in the disturbances.

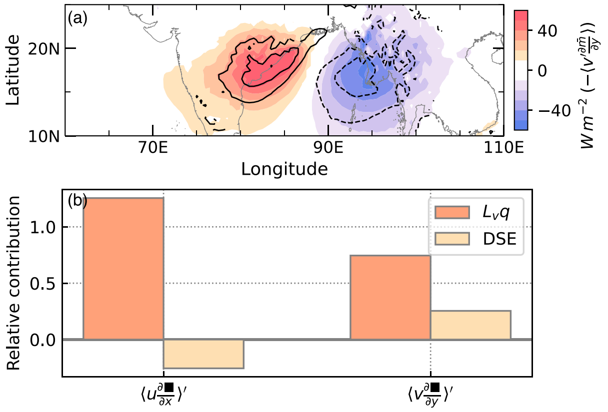

FIG. 9. (a) $-\langle v(\partial m/\partial y)\rangle'$ (contours, from -50 to 50 W m^{-2} at an interval of 10 W m^{-2}) and $-\langle v'(\partial\overline{m}/\partial y)\rangle$ (shading) regressed onto the MLPS index on day 0. (b) Relative contributions of the column-integrated horizontal advection of latent energy and DSE to the horizontal MSE advection.

The column-integrated perturbation kinetic energy tendency can be split into the following terms (Maloney and Hartmann 2001; Maloney and Dickinson 2003; Diaz and Boos 2019a,b):

$$\frac{\partial\langle K'\rangle}{\partial t} = -\langle\overline{\mathbf{v}}\cdot\nabla_h K'\rangle - \left\langle\overline{\omega}\frac{\partial K'}{\partial p}\right\rangle - \langle\mathbf{v}'\cdot\nabla_h K'\rangle - \left\langle\omega'\frac{\partial K'}{\partial p}\right\rangle - \langle\mathbf{v}'\cdot\nabla_h\Phi'\rangle + \langle C_b\rangle + \langle C_{bV}\rangle - \langle D\rangle, \qquad (7)$$

where $\overline{\mathbf{v}}\cdot\nabla_h K'$ is the horizontal advection of PKE,

$$C_b \equiv -u'v'\left(\frac{\partial\overline{v}}{\partial x} + \frac{\partial\overline{u}}{\partial y}\right) - u'^2\frac{\partial\overline{u}}{\partial x} - v'^2\frac{\partial\overline{v}}{\partial y} \qquad (8)$$

is the barotropic energy conversion along the horizontal plane,

$$C_{bV} \equiv -u'\omega'\frac{\partial\overline{u}}{\partial p} - v'\omega'\frac{\partial\overline{v}}{\partial p} \qquad (9)$$

is the vertical barotropic energy conversion, and

$$\mathbf{v}'\cdot\nabla_h\Phi' = u'\frac{\partial\Phi'}{\partial x} + v'\frac{\partial\Phi'}{\partial y} \qquad (10)$$

is the geopotential advection by the anomalous horizontal winds, indicating the work done by the pressure gradient force (Diaz and Boos 2019b). The term D' is the sum of friction and other processes. Since we are unable to calculate the friction using reanalysis data, we put friction and other processes that cannot be inferred from the current dataset into the residual ("res") between the left-hand side and the right-hand side. The relative share of each term is shown in Fig. 11, which is calculated following Eq. (5).

As shown in Fig. 11, the major contributors to the PKE tendency are the horizontal advection of anomalous geopotential by the wind anomalies ($\mathbf{v}'\cdot\nabla_h\Phi'$) and the budget residual. The budget residual projects positively to the PKE tendency, indicating that the residual is not only a result of dissipation but may also be the result of processes that are unsolved in the reanalysis data, possibly related to subgrid-scale processes (Diaz and Boos 2019b) or convective systems and internal gravity waves caused by mountains (Alaka and Maloney 2014; Chen et al. 2016). The other terms have relatively small values. The horizontal advection of PKE by anomalous winds, however, shows a nonnegligible increase on day -2 and day 2 and a decrease on day 0. The leading terms to the maintenance of K' are the

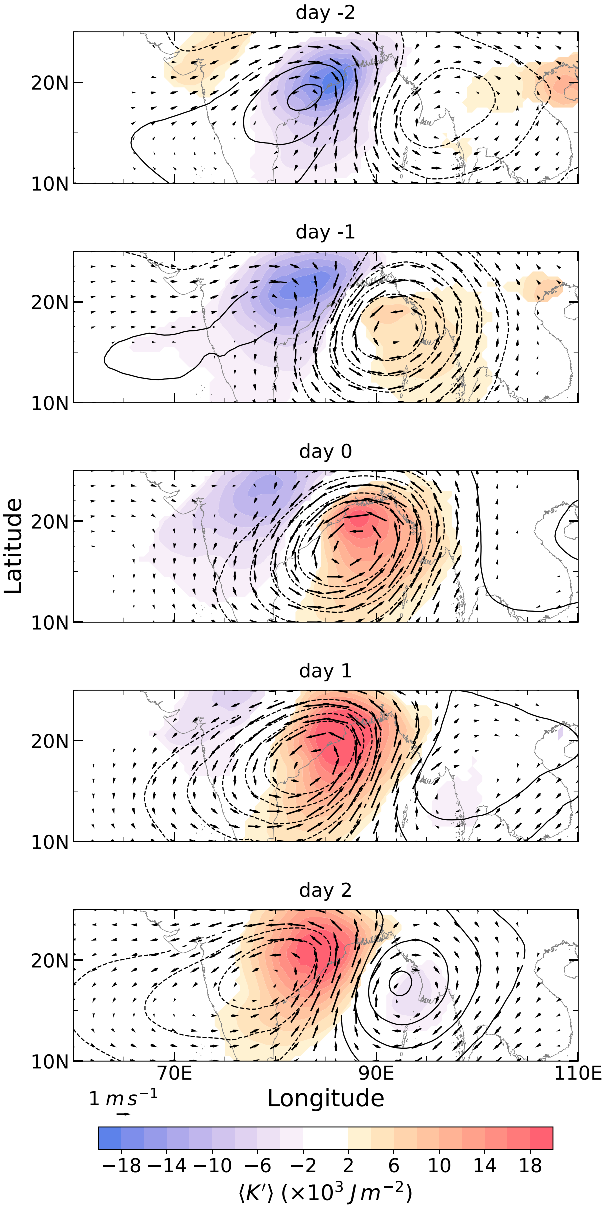

FIG. 10. Lag regressions from day -2 to day 2 of column-integrated perturbation kinetic energy anomalies (shadings), geopotential height (contours, from -4 to 4 gpm at an interval of 1 gpm), and winds (vectors) at 500 hPa onto the MLPS index. Only statistically significant anomalies are shown.

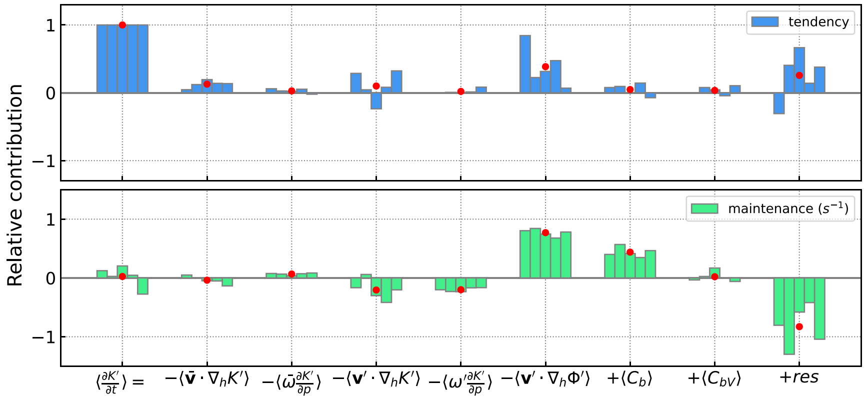

FIG. 11. Normalized contributions to (top) PKE tendency ($\partial \langle K' \rangle / \partial t$)) and (bottom) maintenance ($\langle K' \rangle$)) from the terms in Eq. (7). "Res" refers to the residual between the left-hand side and the right-hand side of Eq. (7). The five bins within each group represent the lag regression at days −2, −1, 0, 1, and 2. The red dots are the averages of the five bins. The contributions are calculated within 60°–110°E, 10°–25°N.

horizontal barotropic energy conversion, horizontal advection of geopotential anomalies, and the residual. The horizontal and vertical advection by anomalous winds serves as small but nonnegligible sinks of PKE.

The barotropic term is shown in the leftmost column in Fig. 12. The locations of negative and positive centers of the barotropic term are identical to the PKE (contours). A strong negative barotropic conversion initiates at the east coast of India and the western Bay of Bengal on day −2, collocated with an anticyclonic anomalous flow. The pattern indicates that kinetic energy transports from eddies to the mean state in the anticyclonic anomalies. As the negative center moves northwestward, a weak positive center (transporting kinetic energy from mean state to disturbances) forms and grows in the northern Bay of Bengal. On day 2, the positive center moves to north India and the negative center disappears.

The horizontal advection of anomalous geopotential by the wind anomalies is shown in the middle column of Fig. 12, which can be viewed as the work done by the pressure gradient force (Diaz and Boos 2019b). From the examination of the composites, it is clear that this term is nearly always in phase with the PKE (contours). Given that the nondivergent component of the winds is parallel to the isobars in MLPSs (Fig. 3), it follows that the positive $\langle \mathbf{v}' \cdot \nabla_h \Phi' \rangle$ anomalies are the result of the strong divergence that is associated with the anomalous convection that is located near the center of the anomalous cyclones and anticyclones (Figs. 3 and 5).

The residual is shown in the rightmost column of Fig. 12. The pattern exhibits more northward propagation than westward propagation. The enhanced residual centers are to the south of the negative PKE tendency and to the north of the positive PKE tendency.

5. Discussion and conclusions

In this study, we created an MLPS index by filtering precipitation data to retain westward-propagating wavenumbers from 3 to 25, and frequencies between 1/2 and 1/15 day^{-1}, and averaging over the head of the Bay of Bengal. The index was used to create lag regressions that elucidated the structure of MLPSs and their governing processes. The regression results were then compared with three theories that have been posited to explain MLPS growth and propagation: dry barotropic, baroclinic, and moisture–vortex growth. The consistency between observations and theories is summarized in Table 1.

We found that none of the theories alone are capable of explaining all the features we found in MLPSs. However, most of them are consistent with the combination of barotropic and MVI-like growth. Thus, we posit that these two mechanisms could be potential explanations for MLPS growth and propagation. Evidence for this statement can be found by revisiting the MSE and PKE budgets. As seen in Fig. 7, the meridional advection of mean MSE by anomalous winds is vital to both the propagation and growth of the MSE anomalies. Longwave radiative heating is also important to the maintenance of MSE, in both MLPSs and other slow-propagating convectively coupled systems across the tropics (Yasunaga et al. 2019; Andersen and Kuang 2012; Mayta et al. 2022). However, this positive feedback is balanced out by the vertical advection of MSE. The anvils caused by the vertical motion suppress the outgoing longwave radiation and hence compensate for the MSE sink from vertical MSE advection (Andersen and Kuang 2012; Adames and Ming 2018b; Inoue et al. 2020). So only when horizontal MSE advection is considered can we explain the growth of MSE within MLPSs. The contributions from horizontal MSE advection to maintenance are approximately equal to the projection from MSE tendency. A positive projection of MSE tendency to maintenance implies an increase in MSE, and a negative projection indicates a decrease.

The examination of the PKE budgets shows that the barotropic conversion from the horizontal shear is important for the maintenance of PKE in MLPSs. The downgradient advection of anomalous geopotential, on the other hand, cannot be explained with barotropic growth. The nondivergent component

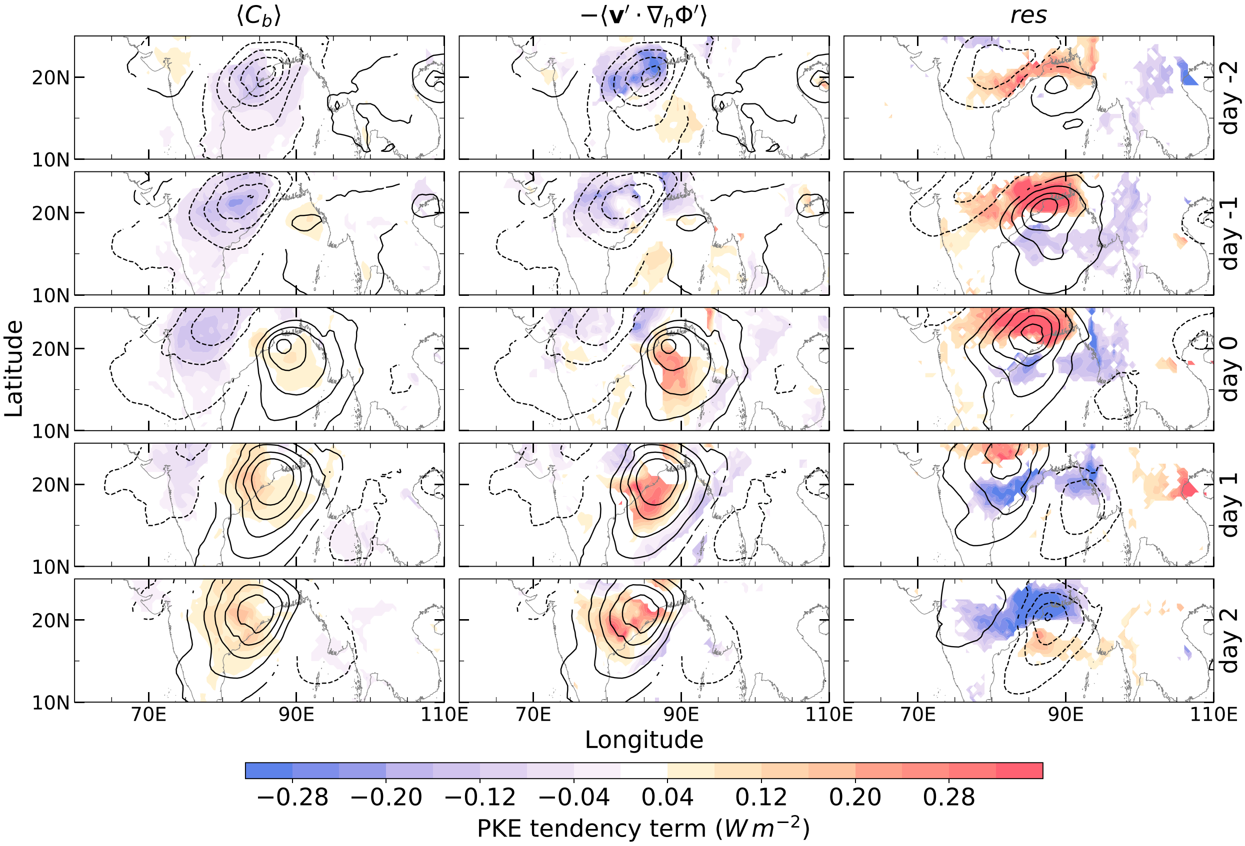

FIG. 12. From top to bottom, the maps are lag regressions from day −2 to day 2. The shading represents (left) the column-integrated horizontal barotropic term ($\langle C_b \rangle$), (center) horizontal geopotential advection ($-\langle \mathbf{v}' \cdot \nabla_h \Phi' \rangle$), and (right) residual (res). The contours in the right column are the tendency of column-integrated PKE ($\partial \langle K' \rangle / \partial t$ from -18×10^3 to 18×10^3 W m^{-2} at an interval of 4×10^3 W m^{-2}), and the contours in the left and center columns are the column-integrated PKE ($\langle K' \rangle$ from −0.2 to 0.25 J m^{-2} at an interval of 0.05 J m^{-2}). Only statistically significant anomalies are shown.

of horizontal winds in MLPSs is approximately geostrophic or gradient wind balance and tends to be parallel to the isobars (Adames 2022). In the absence of convection, these winds can induce barotropic growth but exhibit a negligible downgradient advection of anomalous geopotential. In MVI, however, winds that blow down the pressure gradient would be explained by the irrotational flow that is brought about by the existence of convection near the center of the MLPS. Thus, this contribution to the PKE maintenance likely comes from MVI-like processes. Together, barotropic energy conversions and downgradient winds can generate enough PKE to maintain MLPSs against sinks.

With barotropic and MVI-like growth being consistent with most of the features of MLPSs, it follows that baroclinic growth does not need to be invoked. Further, most of the features of MLPSs disagree with this type of growth, such as the upright structure, and collocating of water vapor, rainfall, and vorticity. This result supports previous works that have posited that baroclinic growth is of little importance to MLPSs (Cohen and Boos 2016; Adames 2021).

TABLE 1. A summary of the features in MLPSs documented in this study and which growth process is consistent with.

Observed feature	MVI-like	Dry barotropic	Moist baroclinic
Upright vertical structure	Yes	Yes	No
Tilts against horizontal shear	No	Yes	No
Synoptic horizontal scale of ∼1000 km	Yes	Yes	Yes
Moisture, precipitation, and vorticity have an in-phase component	Yes	No	No
MSE anomalies follow the contours of mean MSE	Yes	No	Yes
Meridional MSE advection important for MSE growth	Yes	No	Yes
Barotropic energy conversion important for PKE generation	No	Yes	No
PKE generation through downgradient geopotential advection	Yes	No	Yes

It is worth noting that the moist barotropic instability mechanism proposed by Diaz and Boos (2019b) has many similarities to MVI. Diaz and Boos (2021a) also posit that meridional MSE advection is essential to MLPS growth. In a way, moist barotropic instability can be viewed as a combination of MVI and dry barotropic instability. Hence, we do not discuss this growth mechanism in Table 1 but acknowledge that it can also explain the observed features of MLPSs.

Caveats and future work

There are a few caveats in this study. Although residuals exist in both MSE and PKE budgets, their contributions are different. The MSE budget residual is negligibly small. The PKE budget residual, however, is significant. It functions as a sink of PKE but acts to propagate the PKE northwestward. Frictional dissipation could be the reason for the vortex decay. Subgrid-scale processes that are not well represented in ERA5, such as convective momentum transports, could account for the contribution to propagation (Chen et al. 2016). Also, the residual may be a result of numerical errors due to the complex topography of the region.

Because we used linear regression to understand MLPSs, our analysis does not account for nonlinearities that may be present in individual systems. Also, the index and the linear regressions emphasize the weaker MLPSs and not the stronger monsoon depressions. The stronger depressions differ from MLPSs in that latent heat fluxes are also important for the growth of depressions (Fujinami et al. 2020; Diaz and Boos 2021b).

In this study, we only present evidence that MSE advection is a key factor in MVI-like growth. Recent work has indicated that the disturbances that grow from MVI extract latent energy from the background circulation (Mayta and Adames Corraliza 2023, manuscript submitted to *J. Climate*; Adames Corraliza and Mayta 2023, manuscript submitted to *J. Climate*). Extending the results to this study would lead to the hypothesis that MLPSs extract latent energy from the Indian monsoon, thereby weakening it. Testing this hypothesis will be the focus of future research.

Acknowledgments. ÁFA and HL were supported by the National Science Foundation AGS-1841559. HL would like to thank Víctor C. Mayta for helping to review and improve the manuscript. The authors also thank anonymous reviewers for their highly constructive suggestions.

Data availability statement. The data used in this study all come from the European Centre for Medium-Range Weather Forecasts. The datasets are available for download at https://cds.climate.copernicus.eu/cdsapp#!/home.

APPENDIX

Index Sensitivity Test

Empirical orthogonal function analysis is applied over the domain shown in Fig. A1. EOF1 explains 14.3% of the total variance, and the pattern is similar to the disturbance growth (day −1 in Fig. 3). EOF2 explains 13.6% of the variance and is similar to the pattern of decay on day 1.

The filtered mean sea level pressure, averaged over the head of the Bay of Bengal (red box in Fig. 2), was also tested as an index (Fig. A2). The disturbance has the same growth and propagation features as the one with precipitation as its index but has a relatively smaller magnitude in rainfall but stronger winds and geopotential anomalies.

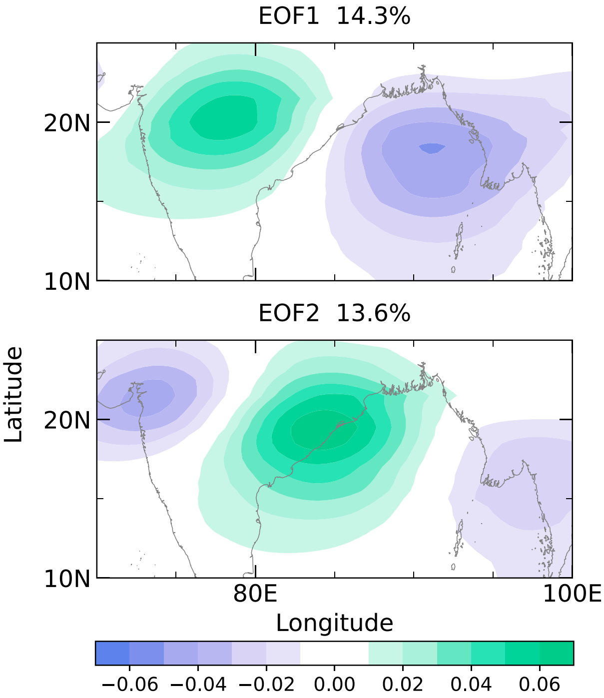

FIG. A1. The leading two EOFs of the filtered precipitation anomalies.

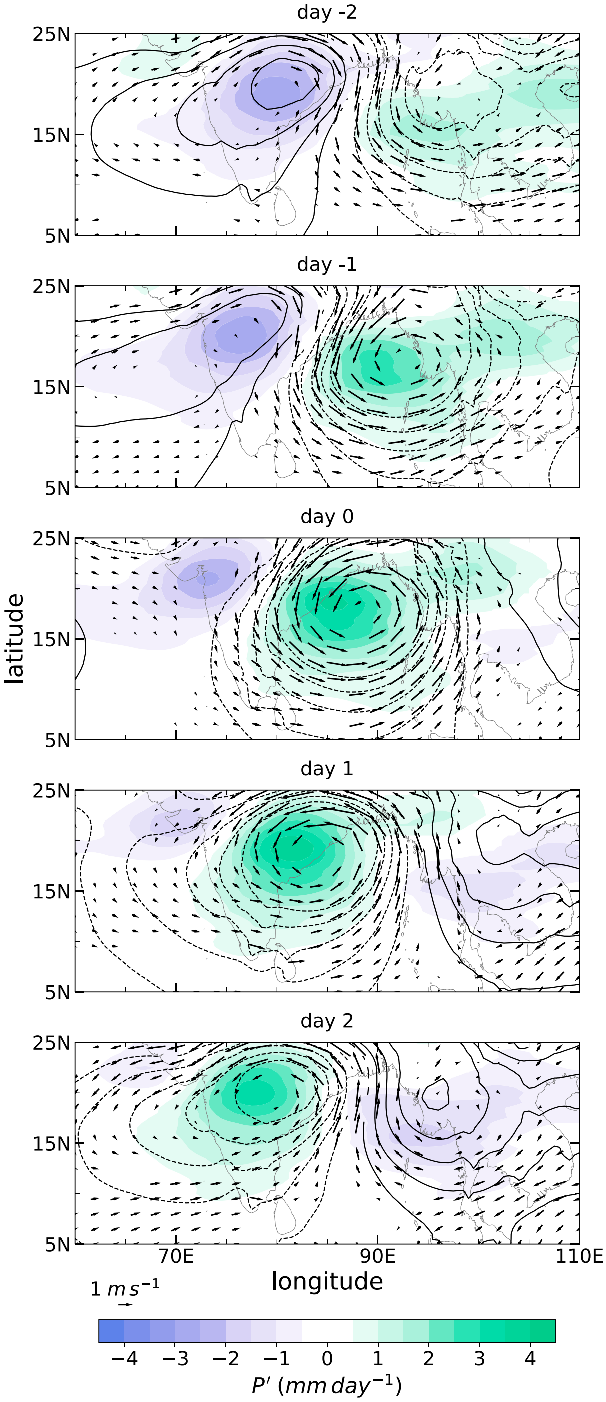

FIG. A2. As in Fig. 3, but using filtered mean SLP as the MLPS index.

REFERENCES

Adames, Á. F., 2021: Interactions between water vapor, potential vorticity, and vertical wind shear in quasi-geostrophic motions: Implications for rotational tropical motion systems. *J. Atmos. Sci.*, **78**, 903–923, https://doi.org/10.1175/JAS-D-20-0205.1.

——, 2022: The basic equations under weak temperature gradient balance: Formulation, scaling, and types of convectively coupled motions. *J. Atmos. Sci.*, **79**, 2087–2108, https://doi.org/10.1175/JAS-D-21-0215.1.

——, and J. M. Wallace, 2014: Three-dimensional structure and evolution of the MJO and its relation to the mean flow. *J. Atmos. Sci.*, **71**, 2007–2026, https://doi.org/10.1175/JAS-D-13-0254.1.

——, and Y. Ming, 2018a: Interactions between water vapor and potential vorticity in synoptic-scale monsoonal disturbances: Moisture vortex instability. *J. Atmos. Sci.*, **75**, 2083–2106, https://doi.org/10.1175/JAS-D-17-0310.1.

——, and ——, 2018b: Moisture and moist static energy budgets of South Asian monsoon low pressure systems in GFDL AM4.0. *J. Atmos. Sci.*, **75**, 2107–2123, https://doi.org/10.1175/JAS-D-17-0309.1.

Ajayamohan, R. S., W. J. Merryfield, and V. V. Kharin, 2010: Increasing trend of synoptic activity and its relationship with extreme rain events over central India. *J. Climate*, **23**, 1004–1013, https://doi.org/10.1175/2009JCLI2918.1.

Alaka, G. J., Jr., and E. D. Maloney, 2014: The intraseasonal variability of African easterly wave energetics. *J. Climate*, **27**, 6559–6580, https://doi.org/10.1175/JCLI-D-14-00146.1.

Andersen, J. A., and Z. Kuang, 2012: Moist static energy budget of MJO-like disturbances in the atmosphere of a zonally symmetric aquaplanet. *J. Climate*, **25**, 2782–2804, https://doi.org/10.1175/JCLI-D-11-00168.1.

Aravéquia, J. A., V. B. Rao, and J. P. Bonatti, 1995: The role of moist baroclinic instability in the growth and structure of monsoon depressions. *J. Atmos. Sci.*, **52**, 4393–4409, https://doi.org/10.1175/1520-0469(1995)052%3C4393:TROMBI%3E2.0.CO;2.

Boos, W. R., J. V. Hurley, and V. S. Murthy, 2015: Adiabatic westward drift of Indian monsoon depressions. *Quart. J. Roy. Meteor. Soc.*, **141**, 1035–1048, https://doi.org/10.1002/qj.2454.

——, B. E. Mapes, and V. S. Murthy, 2016: Potential vorticity structure and propagation mechanism of Indian monsoon depressions. *The Global Monsoon System*, World Scientific Series on Asia-Pacific Weather and Climate, Vol. 9, World Scientific, 187–199, https://doi.org/10.1142/9789813200913_0015.

Charney, J. G., and M. E. Stern, 1962: On the stability of internal baroclinic jets in a rotating atmosphere. *J. Atmos. Sci.*, **19**, 159–172, https://doi.org/10.1175/1520-0469(1962)019<0159:OTSOIB>2.0.CO;2.

Chen, B., W.-w. Tung, and M. Yanai, 2016: Multiscale temporal mean features of perturbation kinetic energy and its budget in the tropics: Review and computation. *Multiscale Convection-Coupled Systems in the Tropics: A Tribute to Dr. Michio Yanai, Meteor. Monogr.*, No. 56, Amer. Meteor. Soc., https://doi.org/10.1175/AMSMONOGRAPHS-D-15-0017.1.

Chen, W. Y., 1982: Fluctuations in Northern Hemisphere 700 mb height field associated with the Southern Oscillation. *Mon. Wea. Rev.*, **110**, 808–823, https://doi.org/10.1175/1520-0493(1982)110<0808:FINHMH>2.0.CO;2.

Clark, S. K., Y. Ming, and Á. F. Adames, 2020: Monsoon low pressure system–like variability in an idealized moist model. *J. Climate*, **33**, 2051–2074, https://doi.org/10.1175/JCLI-D-19-0289.1.

Cohen, N. Y., and W. R. Boos, 2016: Perspectives on moist baroclinic instability: Implications for the growth of monsoon depressions. *J. Atmos. Sci.*, **73**, 1767–1788, https://doi.org/10.1175/JAS-D-15-0254.1.

Davis, R. E., 1978: Predictability of sea level pressure anomalies over the North Pacific Ocean. *J. Phys. Oceanogr.*, **8**, 233–246, https://doi.org/10.1175/1520-0485(1978)008<0233:POSLPA>2.0.CO;2.

Diaz, M., and W. R. Boos, 2019a: Barotropic growth of monsoon depressions. *Quart. J. Roy. Meteor. Soc.*, **145**, 824–844, https://doi.org/10.1002/qj.3467.

——, and ——, 2019b: Monsoon depression amplification by moist barotropic instability in a vertically sheared environment. *Quart. J. Roy. Meteor. Soc.*, **145**, 2666–2684, https://doi.org/10.1002/qj.3585.

——, and ——, 2021a: Evolution of idealized vortices in monsoon-like shears: Application to monsoon depressions. *J. Atmos. Sci.*, **78**, 1207–1225, https://doi.org/10.1175/JAS-D-20-0286.1.

——, and ——, 2021b: The influence of surface heat fluxes on the growth of idealized monsoon depressions. *J. Atmos. Sci.*, **78**, 2013–2027, https://doi.org/10.1175/JAS-D-20-0359.1.

Ditchek, S. D., W. R. Boos, S. J. Camargo, and M. K. Tippett, 2016: A genesis index for monsoon disturbances. *J. Climate*, **29**, 5189–5203, https://doi.org/10.1175/JCLI-D-15-0704.1.

Dong, W., Y. Lin, J. S. Wright, Y. Xie, F. Xu, W. Xu, and Y. Wang, 2017: Indian monsoon low-pressure systems feed up-and-over moisture transport to the southwestern Tibetan Plateau. *J. Geophys. Res. Atmos.*, **122**, 12 140–12 151, https://doi.org/10.1002/2017JD027296.

Fujinami, H., H. Hirata, M. Kato, and K. Tsuboki, 2020: Mesoscale precipitation systems and their role in the rapid development of a monsoon depression over the Bay of Bengal. *Quart. J. Roy. Meteor. Soc.*, **146**, 267–283, https://doi.org/10.1002/qj.3672.

Godbole, R. V., 1977: The composite structure of the monsoon depression. *Tellus*, **29A**, 25–40, https://doi.org/10.3402/tellusa.v29i1.11327.

Hayashi, Y., 1971: A generalized method of resolving disturbances into progressive and retrogressive waves by space Fourier and time cross-spectral analyses. *J. Meteor. Soc. Japan*, **49**, 125–128, https://doi.org/10.2151/jmsj1965.49.2_125.

——, 1979: A generalized method of resolving transient disturbances into standing and traveling waves by space-time spectral analysis. *J. Atmos. Sci.*, **36**, 1017–1029, https://doi.org/10.1175/1520-0469(1979)036<1017:AGMORT>2.0.CO;2.

Hersbach, H., and Coauthors, 2019: Global reanalysis: Goodbye ERA-Interim, hello ERA5. *ECMWF Newsletter*, No. 159, ECMWF, Reading, United Kingdom, 17–24, https://doi.org/10.21957/vf291hehd7.

Hunt, K. M. R., and J. K. Fletcher, 2019: The relationship between Indian monsoon rainfall and low-pressure systems. *Climate Dyn.*, **53**, 1859–1871, https://doi.org/10.1007/s00382-019-04744-x.

——, A. G. Turner, P. M. Inness, D. E. Parker, and R. C. Levine, 2016: On the structure and dynamics of Indian monsoon depressions. *Mon. Wea. Rev.*, **144**, 3391–3416, https://doi.org/10.1175/MWR-D-15-0138.1.

——, ——, and L. C. Shaffrey, 2018: Extreme daily rainfall in Pakistan and north India: Scale interactions, mechanisms, and precursors. *Mon. Wea. Rev.*, **146**, 1005–1022, https://doi.org/10.1175/MWR-D-17-0258.1.

Inoue, K., Á. F. Adames, and K. Yasunaga, 2020: Vertical velocity profiles in convectively coupled equatorial waves and MJO: New diagnoses of vertical velocity profiles in the wavenumber–frequency domain. *J. Atmos. Sci.*, **77**, 2139–2162, https://doi.org/10.1175/JAS-D-19-0209.1.

Kasture, S. V., R. N. Keshavamurty, and V. Satyan, 1993: A model study of the growth of summer monsoon disturbances. *Curr. Sci.*, **64**, 673–679.

Krishnakumar, V., R. N. Keshavamurty, and S. V. Kasture, 1992: Moist baroclinic instability and the growth of monsoon depressions—Linear and nonlinear studies. *Proc. Indian Acad. Sci., Earth Planet. Sci.*, **101**, 123–152, https://doi.org/10.1007/BF02840349.

Krishnamurthy, V., and R. S. Ajayamohan, 2010: Composite structure of monsoon low pressure systems and its relation to Indian rainfall. *J. Climate*, **23**, 4285–4305, https://doi.org/10.1175/2010JCLI2953.1.

Krishnamurti, T. N., 1979: *Tropical Meteorology*. World Meteorological Organization, 428 pp.

——, M. Kanamitsu, R. Godbole, C.-B. Chang, F. Carr, and J. H. Chow, 1975: Study of a monsoon depression (I). *J. Meteor. Soc. Japan*, **53**, 227–240, https://doi.org/10.2151/jmsj1965.53.4_227.

——, ——, ——, ——, ——, and ——, 1976: Study of a monsoon depression (II), dynamical structure. *J. Meteor. Soc. Japan*, **54**, 208–225, https://doi.org/10.2151/jmsj1965.54.4_208.

——, A. Martin, R. Krishnamurti, A. Simon, A. Thomas, and V. Kumar, 2013: Impacts of enhanced CCN on the organization of convection and recent reduced counts of monsoon depressions. *Climate Dyn.*, **41**, 117–134, https://doi.org/10.1007/s00382-012-1638-z.

Lindzen, R. S., B. Farrell, and A. J. Rosenthal, 1983: Absolute barotropic instability and monsoon depressions. *J. Atmos. Sci.*, **40**, 1178–1184, https://doi.org/10.1175/1520-0469(1983)040<1178:ABIAMD>2.0.CO;2.

Maloney, E. D., and D. L. Hartmann, 2001: The Madden–Julian oscillation, barotropic dynamics, and North Pacific tropical cyclone formation. Part I: Observations. *J. Atmos. Sci.*, **58**, 2545–2558, https://doi.org/10.1175/1520-0469(2001)058<2545:TMJOBD>2.0.CO;2.

——, and M. J. Dickinson, 2003: The intraseasonal oscillation and the energetics of summertime tropical western North Pacific synoptic-scale disturbances. *J. Atmos. Sci.*, **60**, 2153–2168, https://doi.org/10.1175/1520-0469(2003)060<2153:TIOATE>2.0.CO;2.

Mayta, V., Á. F. Adames, and F. Ahmed, 2022: Westward-propagating moisture mode over the tropical Western Hemisphere. *Geophys. Res. Lett.*, **49**, e2022GL097799, https://doi.org/10.1029/2022GL097799.

Moorthi, S., and A. Arakawa, 1985: Baroclinic instability with cumulus heating. *J. Atmos. Sci.*, **42**, 2007–2031, https://doi.org/10.1175/1520-0469(1985)042<2007:BIWCH>2.0.CO;2.

Nitta, T., and K. Masuda, 1981: Observational study of a monsoon depression developed over the Bay of Bengal during summer MONEX. *J. Meteor. Soc. Japan*, **59**, 672–682, https://doi.org/10.2151/jmsj1965.59.5_672.

Rao, K. V., and S. Rajamani, 1970: Diagnostic study of a monsoon depression by geostrophic baroclinic model. *Mausam*, **21**, 187–194, https://doi.org/10.54302/mausam.v21i2.5366.

Saha, K., and C.-P. Chang, 1983: The baroclinic processes of monsoon depressions. *Mon. Wea. Rev.*, **111**, 1506–1514, https://doi.org/10.1175/1520-0493(1983)111<1506:TBPOMD>2.0.CO;2.

——, F. Sanders, and J. Shukla, 1981: Westward propagating predecessors of monsoon depressions. *Mon. Wea. Rev.*, **109**, 330–343, https://doi.org/10.1175/1520-0493(1981)109<0330:WPPOMD>2.0.CO;2.

Sikka, D. R., 1977: Some aspects of the life history, structure and movement of monsoon depressions. *Pure Appl. Geophys.*, **115**, 1501–1529, https://doi.org/10.1007/BF00874421.

Sobel, A. H., J. Nilsson, and L. M. Polvani, 2001: The weak temperature gradient approximation and balanced tropical moisture waves. *J. Atmos. Sci.*, **58**, 3650–3665, https://doi.org/10.1175/1520-0469(2001)058<3650:TWTGAA>2.0.CO;2.

Thomas, T. M., G. Bala, and V. V. Srinivas, 2021: Characteristics of the monsoon low pressure systems in the Indian subcontinent and the associated extreme precipitation events. *Climate Dyn.*, **56**, 1859–1878, https://doi.org/10.1007/s00382-020-05562-2.

——, ——, and S. V. Vemavarapu, 2022: CESM simulation of monsoon low pressure systems over India. *Int. J. Climatol.*, **42**, 5964–5984, https://doi.org/10.1002/joc.7571.

Wheeler, M., and G. N. Kiladis, 1999: Convectively coupled equatorial waves: Analysis of clouds and temperature in the wavenumber–frequency domain. *J. Atmos. Sci.*, **56**, 374–399, https://doi.org/10.1175/1520-0469(1999)056<0374:CCEWAO>2.0.CO;2.

——, ——, and P. J. Webster, 2000: Large-scale dynamical fields associated with convectively coupled equatorial waves. *J. Atmos. Sci.*, **57**, 613–640, https://doi.org/10.1175/1520-0469(2000)057<0613:LSDFAW>2.0.CO;2.

Wolding, B. O., E. D. Maloney, and M. Branson, 2016: Vertically resolved weak temperature gradient analysis of the Madden-Julian oscillation in SP-CESM. *J. Adv. Model. Earth Syst.*, **8**, 1586–1619, https://doi.org/10.1002/2016MS000724.

Yasunaga, K., S. Yokoi, K. Inoue, and B. E. Mapes, 2019: Space–time spectral analysis of the moist static energy budget equation. *J. Climate*, **32**, 501–529, https://doi.org/10.1175/JCLI-D-18-0334.1.

Yoon, J.-H., and T.-C. Chen, 2005: Water vapor budget of the Indian monsoon depression. *Tellus*, **57A**, 770–782, https://doi.org/10.3402/tellusa.v57i5.14737.

——, and W.-R. Huang, 2012: Indian monsoon depression: Climatology and variability. *Modern Climatology*, IntechOpen, 45–72, https://doi.org/10.5772/37917.